

RELATIONSHIPS BETWEEN CHARACTERISTICS OF THE LINE-OF-SIGHT MAGNETIC FIELD AND SOLAR FLARE FORECASTS

VIACHESLAV M SADYKOV^{1,2} AND ALEXANDER G KOSOVICHEV^{1,2,3}

¹*Center for Computational Heliophysics, New Jersey Institute of Technology, Newark, NJ 07102, USA*

²*Department of Physics, New Jersey Institute of Technology, Newark, NJ 07102, USA*

³*NASA Ames Research Center, Moffett Field, CA 94035, USA*

ABSTRACT

Studying connection between solar flares and properties of magnetic field in active regions is very important for understanding the flare physics and developing space weather forecasts. In this work, we analyze relationship between the flare X-ray peak flux from the GOES satellite, and characteristics of the line-of-sight (LOS) magnetograms obtained by the SDO/HMI instrument during the period of April, 2010 — June, 2016. We try to answer two questions: 1) What characteristics of the LOS magnetic field are most important for the flare initiation and magnitude? 2) Is it possible to construct a reliable forecast of $\geq M1.0$ and $\geq X1.0$ class flares based only on the LOS magnetic field characteristics? To answer these questions, we apply a Polarity Inversion Line (PIL) detection algorithm, and derive various properties of the PIL and the corresponding Active Regions (AR). The importance of these properties for flare forecasting is determined by their ability to separate flaring cases from non-flaring, and their Fisher ranking score. It is found that the PIL characteristics are of special importance for the forecasts of both $\geq M1.0$ and $\geq X1.0$ flares, while the global AR characteristics become comparably discriminative only for $\geq X1.0$ flares. We use the Support Vector Machine (SVM) classifier and train it on the six characteristics of the most importance for each case.

The obtained True Skill Statistics (TSS) values of 0.70 for $\geq M1.0$ flares and 0.64 for $\geq X1.0$ flares are better than the currently-known expert-based predictions. Therefore, the results confirm the importance of the LOS magnetic field data and, in particular, the PIL region characteristics for flare forecasts.

Keywords: methods: statistical — Sun: activity — Sun: flares — Sun: magnetic fields

1. INTRODUCTION

Usually lasting from several minutes to several hours, solar flares can release more than 10^{32} erg of energy, and cause harmful effects to the terrestrial environment. The only possible source to accumulate such large amounts of energy is magnetic field of active regions. [Emslie et al. \(2012\)](#) demonstrated for a sample of 38 flares that the total energy of non-potential magnetic field was sufficient to explain the flare energy release including Coronal Mass Ejections (CMEs), energetic particles, and hot plasma emission and dynamics. For understanding the flare physical mechanism and flare prediction it is important to find critical magnetic field characteristics that are linked to the flare initiation and strength.

There have been two types of such study. The first type is focused on global characteristics of active regions, and the second approach is to search for local critical properties of magnetic fields. For instance, in the first type studies, [Mandage & McAteer \(2016\)](#) demonstrated a difference between the magnetic field power spectrum slopes of flaring and non-flaring active regions. [Bobra & Couvidat \(2015\)](#) calculated different descriptors of vector magnetograms of active regions, and applied machine-learning techniques for a flare prediction algorithm. Also, a recent study of [Raboonik et al. \(2016\)](#) used the Zerneke moments as characteristics of the active region magnetic field for flare prediction.

Many observational studies of the second type confirmed the important role of the magnetic field Polarity Inversion Line (PIL) in the flare activity (e.g. [Severny 1964](#); [Hagyard et al. 1990](#); [Wang et al. 1994](#); [Falconer et al. 1997](#); [Kosovichev and Zharkova 2001](#); [Jing et al. 2006](#); [Schrijver 2007](#); [Kumar et al. 2015](#); [Barnes et al. 2016](#); [Sharykin et al. 2016](#)). From magnetograms in the PIL vicinity, one can extract several descriptors representing the local field. For example, [Falconer et al. \(2003\)](#) showed that the length of the PIL with strong field gradient and sheared transverse field correlates with the CME and flare productivity. [Mason & Hoeksema \(2010\)](#) introduced the Gradient-Weighted PIL length as a characteristic for solar flare forecast. [Falconer et al. \(2011, 2012, 2014\)](#) found that this characteristic is a good proxy for the magnetic free energy. [Leka & Barnes \(2003a,b, 2007\)](#) considered the shear angle between the observed and reconstructed magnetic fields.

Chernyshov et al. (2011) used the PIL length, the area of strong field in the PIL vicinity, and the total flux in this area, as well as the rates of these characteristics.

In this paper, we perform a critical analysis of correlation between different line-of-sight (LOS) magnetic field characteristics (derived from the entire active region and from the PIL vicinity) and flare activity, and consider the importance of LOS observations for flare forecast. Such analysis based on the LOS magnetograms is important because these observations are routinely performed by various space-based and ground-based observatories. In Section 2, we describe automatic procedures for magnetogram segmentation, identification of PIL, and calculation of various magnetic field characteristics. In Section 3, we investigate relationships between the derived characteristics and the occurrence of $\geq M1.0$ and $\geq X1.0$ class solar flares. Section 4 describes the application of Support Vector Machine (SVM) classifier to predict M- and X-class flares based on the LOS characteristics. Our conclusions are summarized in Section 5.

2. MAGNETOGRAM SEGMENTATION AND DERIVATION OF CHARACTERISTICS

For analysis we used the Line-of-Sight (LOS) magnetograms of active regions, obtained by the Helioseismic and Magnetic Imager onboard the Solar Dynamics Observatory (SDO/HMI, Scherrer et al. 2012). The active region data were represented in the form of $30^\circ \times 30^\circ$ data cubes with 1 h cadence, remapped onto the heliographic coordinates using the Postel’s projection, and tracked with the solar differential rotation during the whole passage of active regions on the solar disc, employing the standard SDO/JSOC software.

By definition, the Polarity Inversion Line (PIL) is the line where the LOS magnetic field changes its sign. For the automatic robust detection of the PIL of strong fields in active regions we use the algorithm initially introduced by Chernyshov et al. (2011) and Laptev (2011). This algorithm is based on a magnetogram segmentation process formulated as an optimization task. The goal is to divide the magnetogram into regions with strong positive field (“positive” segments), strong negative field (“negative” segments), or weak field (“neutral” segments).

Suppose B is a magnetic field strength map, Z_i is a pixel i class (i.e. “positive”, “negative” or “neutral”), N is the total number of pixels, $\varepsilon(i)$ is a neighborhood (e.g. the closest 8 pixels) of pixel

i. The magnetogram segmentation can be formulated as the following optimization procedure to maximize function $p(B|Z)$:

$$p(B|Z) \propto \prod_{i=1}^N \phi_i(Z_i, B_i) \prod_{j \in \varepsilon(i)} \phi(Z_i, Z_j) \rightarrow \max(Z).$$

Here $\phi_i(Z_i, B_i)$ and $\phi(Z_i, Z_j)$ are the scoring functions for each pixel depending on the magnetic field strength and assumed classes of pixels. The choice of the scoring function defines segmentation characteristics and, in fact, should do the following: separate the segments of positive and negative magnetic field polarity, and avoid very small segments with weak field probably coming from noise in the data. We use the scoring functions suggested by [Chernyshov et al. \(2011\)](#):

$$\begin{aligned} \phi_i(Z_i, B_i) &= e^{-C_1 \sqrt{|B_0 - B_i|}}, \text{ for } Z_i \text{ "positive"} \\ \phi_i(Z_i, B_i) &= e^{-C_1 \sqrt{|B_0 + B_i|}}, \text{ for } Z_i \text{ "negative"} \\ \phi_i(Z_i, B_i) &= e^{-C_2 |B_i|}, \text{ for } Z_i \text{ "neutral"} \\ \phi(Z_i, Z_j) &= e^{C_{pair} [Z_i \neq Z_j]}, \end{aligned}$$

where parameters $C_1 = 1.0$, $C_2 = 1.0$, $C_{pair} = 20$, $B_0 = 1000$ G are chosen to obtain a stable segmentation of magnetic polarities in strong field regions. Here $[Z_i \neq Z_j]$ is equal 1 if $Z_i \neq Z_j$, and zero otherwise. Following [Laptev \(2011\)](#), the distribution $p(B|Z)$ is approximated by the factorized distribution $q(Z) = \prod_{i=1}^n q_i(Z_i)$. One can find the factorized distribution, $q(Z)$, closest to $p(B|Z)$ by minimizing the Kullback-Leibler (KL) divergence ([Bishop 2006](#)) of the distributions:

$$KL(q||p) = - \int q(Z) \log \frac{p(B|Z)}{q(Z)} dZ \rightarrow \min(q(Z))$$

The optimal $q(Z)$ is given by solution of the following equation:

$$q_i(Z_i) = \frac{1}{C} \exp(\log(\phi_i(Z_i)) - C_{pair} \sum_{t \in \varepsilon(i)} \sum_{j \neq i} q_j(Z_j))$$

which can be found iteratively:

$$q_i^{new}(Z_i) = \frac{1}{C} \exp(\log(\phi_i(Z_i)) - C_{pair} \sum_{t \in \varepsilon(i)} \sum_{j \neq i} q_j^{old}(Z_j))$$

Using this equation, one can calculate the factorized distribution multiplier q_i for each pixel i and its assumed class Z_i ("positive", "negative", or "neutral"). Because the factorized distribution

represents the product of multipliers for each pixel, one can simply maximize $q_i(Z_i)$ for each pixel i separately.

For identification of PIL in active regions, we smooth the original HMI magnetogram using the Gaussian filter with width $\sigma = 1.5''$, and apply the segmentation algorithm. Then, we apply a morphological dilation procedure separately for positive and negative segments (i.e. expand each segment to include neighboring pixels), and find the PIL as an intersection of the dilated positive and negative segments. Finally, we filter all small islands of the PIL with the number of pixels less than 3% of the total number of pixels occupied by PIL. This approach is quite robust, and allows us to automatically identify the PIL and calculate magnetic field properties. An example of the segmentation and PIL detection for the AR 11158 is illustrated in Fig. 1.

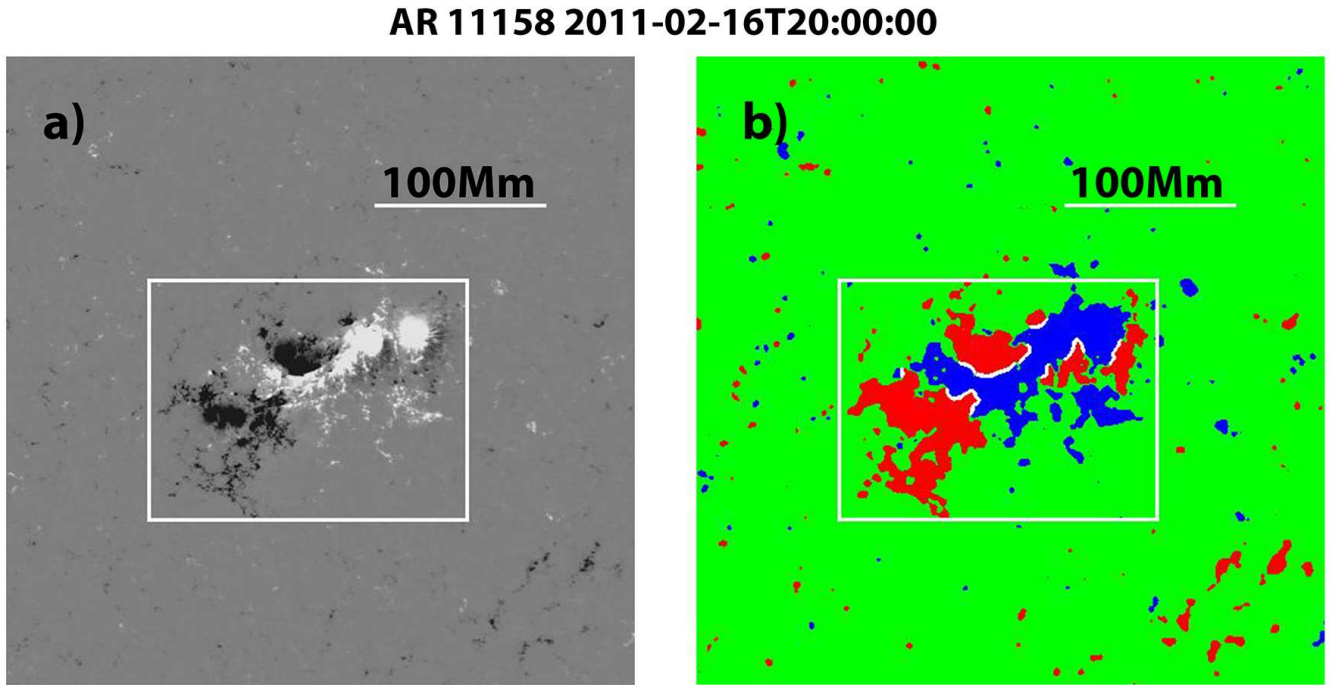


Figure 1. a) The magnetogram of AR 11158 at 2011-02-16 20:00:00 UT. b) The magnetogram segmentation and identification of PIL (red, green, and blue areas correspond to negative, neutral and positive segments). The PIL is shown by white curves.

To isolate the active region area, we use the following two algorithms. The first one is based on the segmentation result: we apply one morphological dilation to the positive/negative segments,

combine them, choose the largest segment containing the active region center, and determine the minimum bounding box around it. The second algorithm is implemented following the procedure of [Stenflo and Kosovichev \(2012\)](#). We have found that the application of both algorithms allows us to separate almost all the ARs from their neighbors. The bounding box extracted for the AR 11158 is presented in Fig. 1.

After performing the segmentation and bounding procedures, we calculate the following descriptors using the derived PIL and the original (non-smoothed) magnetogram:

1. The PIL length. It is defined as the number of pixels occupied by the PIL.
2. The PIL area obtained after 10 morphological dilations of the PIL.
3. The unsigned magnetic flux in the PIL area.
4. The unsigned horizontal gradient in the PIL area defined as sum of $\nabla_h B_z = \sqrt{\left(\frac{\partial B_z}{\partial x}\right)^2 + \left(\frac{\partial B_z}{\partial y}\right)^2}$ over the PIL area pixels.
5. The maximum gradient of the LOS magnetic field across the PIL.
6. The gradient-weighted PIL length as defined by [Mason & Hoeksema \(2010\)](#). The characteristic is calculated as the sum of the PIL pixels multiplied by the unsigned horizontal gradient in each pixel.
7. The R-mask as described by [Schrijver \(2007\)](#). It represents the unsigned magnetic flux weighted with the inverse distance from the PIL.

Also, we calculate the following characteristics of the entire AR (“global” characteristics):

8. The AR area defined as the total area of the positive and negative segments.
9. The unsigned magnetic flux in the AR area.
10. The maximum strength of magnetic field in the AR.
11. The unsigned horizontal gradient in the AR area.

Table 1. Relationship between magnetic field characteristics and flares for $\geq M1.0$ and $\geq X1.0$ class solar flares

Characteristic	Average value ($\geq M1.0$)	Average value ($\geq X1.0$)	5% threshold ($\geq M1.0$)	5% threshold ($\geq X1.0$)
PIL length, Mm	87 ± 42	92 ± 35	17.0	36.0
Area of PIL vicinity, Mm^2	2300 ± 800	2320 ± 780	854	1200
Total flux at PIL vicinity, $G \cdot Mm^2$	$(600 \pm 330) \cdot 10^3$	$(660 \pm 300) \cdot 10^3$	$120 \cdot 10^3$	$268 \cdot 10^3$
Total horizontal gradient at PIL vicinity, $G \cdot Mm$	$(360 \pm 180) \cdot 10^3$	$(370 \pm 140) \cdot 10^3$	$87 \cdot 10^3$	$193 \cdot 10^3$
Maximum gradient across PIL, G/Mm	1000 ± 410	1010 ± 250	360	528
Gradient-weighted PIL length, $Mm \cdot G/Mm$	$(26 \pm 17) \cdot 10^3$	$(27 \pm 12) \cdot 10^3$	2900	8030
R-mask, $G \cdot Mm^2$	$(19 \pm 13) \cdot 10^3$	$(22 \pm 11) \cdot 10^3$	2000	7140
Total AR area, Mm^2	$(11.4 \pm 4.9) \cdot 10^3$	$(12.9 \pm 5.2) \cdot 10^3$	3300	8650
Total AR flux, $G \cdot Mm^2$	$(2700 \pm 1600) \cdot 10^3$	$(3400 \pm 1800) \cdot 10^3$	$580 \cdot 10^3$	$1816 \cdot 10^3$
Maximum field in the AR, G	1750 ± 480	1810 ± 430	1020	1290
Total horizontal gradient in the AR, $G \cdot Mm$	$(1560 \pm 750) \cdot 10^3$	$(1780 \pm 760) \cdot 10^3$	$410 \cdot 10^3$	$882 \cdot 10^3$

3. RELATIONSHIP BETWEEN PIL PROPERTIES AND FLARES

For each $\geq M1.0$ class flare event we consider the magnetograms (remapped onto the heliographic coordinates) observed during one-hour periods 24 h and 1 h prior the flare start time (the corresponding time intervals are 24-25 h and 0-1 h prior the flare start), and calculate the LOS magnetic field characteristics. We plot these characteristics as 1D-histograms for the selected time intervals. Examples of these histograms for the $\geq M1.0$ and $\geq X1.0$ class flares are presented in Fig. 2. The average values of the characteristics in these histograms for the 1 h periods are summarized in Table 1. One can see that these values are just slightly higher for the X-class flare histograms, which complicates the distinction between the M-class and X-class flares.

We have also found one more common feature for all the histograms plotted. The flares are expected only if the characteristics reach some critical (threshold) value. For some LOS characteristics the existence of the critical values is more prominent in the normal-scaled histogram, for others — in the logarithmic-scaled. This common feature may be used to simplify the classification (prediction) problem. The red dashed lines in Fig. 2 represent the threshold values, above which 95% of flares occurred (the threshold is calculated for both 24 h and 1 h periods). Please note that the threshold values are determined only for a subset of ARs, which we will call the “train” dataset and discuss later in Sec. 4. The threshold values for the different characteristics are also summarized in Table 1.

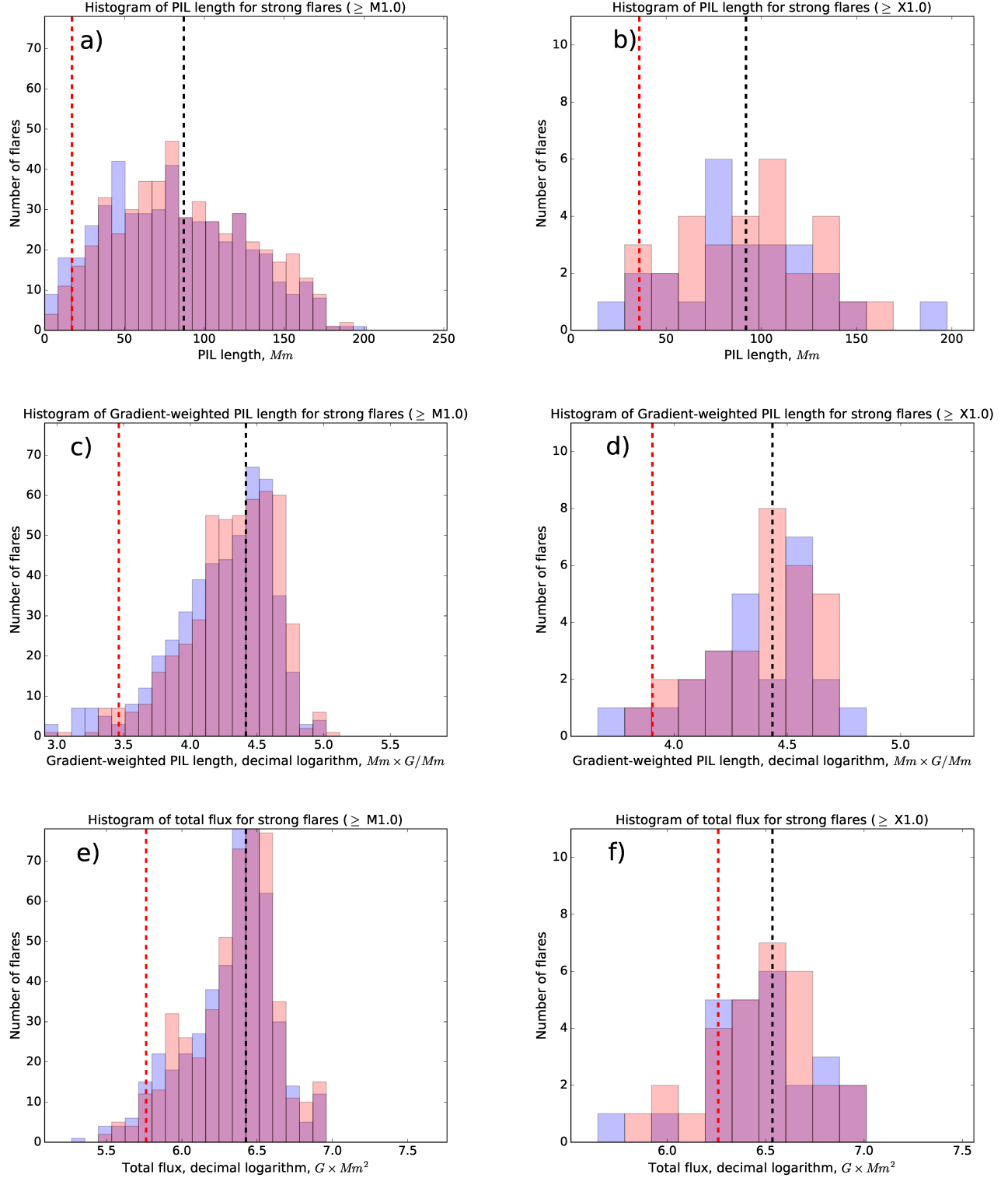


Figure 2. 1D-histograms of the PIL length (a,b), Gradient-Weighted PIL (c,d), and unsigned magnetic flux (e,f) for $\geq M1.0$ class (left panels) and $\geq X1.0$ class (right panels) flares. The parameters are measures 25-24 hours (red histograms) and 1-0 hours (blue histograms) before the flares. The dashed vertical line represents the mean value of the characteristics, the dashed red line shows the threshold values used for the train data set.

4. PREDICTION OF $\geq M1.0$ CLASS SOLAR FLARES

Currently most flare forecasts are based on expert decision. However, the recent works by [Bobra & Couvidat \(2015\)](#) and [Nishizuka et al. \(2017\)](#) demonstrated that the Machine-Learning algorithms may be successfully applied for the flare prediction, resulting in high forecasting scores. These studies demonstrated that descriptors derived from vector magnetic field, such as magnetic helicity, are important for flare prediction. However, the line-of-sight magnetic field data are obtained more regularly, and in near-real time. Therefore, we decided to test if it is possible to forecast $\geq M 1.0$ and $\geq X 1.0$ flares, based solely on the LOS magnetic field characteristics, and among them determine the most discriminative ones.

In this Section we describe the Machine-Learning procedure using the magnetic field characteristics calculated every hour, and the information from the GOES flare catalog. First, we define the positive and negative classes (flaring and non-flaring samples), associating the flare events with the magnetic field characteristics prior the flares. Second, we analyze the characteristics and select the most important ones for separation of the positive and negative classes. Third, we set up the Support Vector Machine classifier (SVM), train it, and run on the “test” subset.

4.1. *Definition of Positive and Negative Classes, and Construction of Datasets for SVM Training and Testing*

Following [Nishizuka et al. \(2017\)](#), we classify a set of magnetic field characteristics as a “positive” case if a $\geq M1.0$ flare occurred in the corresponding AR within 24 h after the field measurement. This means that for each flare there can be 24 positive cases (sets of measured LOS magnetic field characteristics) or less.

[Ahmed et al. \(2013\)](#) introduced two ways to determine the negative cases, described by so-called “operational” and “segmented” associations of active region characteristics and flares. According to the operational association, the negative cases are defined to be exactly opposite to the positive cases, i.e. are assigned if there was no flare of $\geq M1.0$ within 24 h after the magnetic field measurement. For the segmented association, the case is thought to be negative if there are no flares occurred within

48 h before and after the case time moment. We use the operational association for the “test” subset while keeping the segmented association for the “train” subset. The segmented association better separates the positive and negative cases (by neglecting negative cases occurring very close to the flare time), while the operational association is needed for real-time predictions.

We divide cases into the “train” and “test” datasets. The “train” dataset is used to tune the classifier, and the “test” dataset simulating real-time data is used to measure the classifier performance afterwards. We randomly selected AR for “train” and “test” subsets, and kept all cases from one AR inside one subset. The ratio of the train and test datasets is approximately 70% to 30% (following [Bobra & Couvidat 2015](#); [Nishizuka et al. 2017](#)).

4.2. Selection of Discriminative Characteristics

The computational cost of SVM is usually estimated as $O(N^2 \times M)$ for $N \gg M$, where N is the number of cases in the train dataset and M is the number of characteristics in each case. It is desirable to decrease both of these numbers. Moreover, inclusion of characteristics that are not discriminative may decrease the performance of the SVM ([Bobra & Couvidat 2015](#)).

Here we use two methods to select the most discriminative characteristics. One of the ways is to calculate the Fisher ranking score (or F-score, [Bobra & Couvidat 2015](#); [Chang & Lin 2008](#)):

$$F(i) = \frac{(\bar{x}_i^+ - \bar{x}_i)^2 + (\bar{x}_i^- - \bar{x}_i)^2}{\frac{1}{n^+ - 1} \sum_{k=1}^{n^+} (x_{k,i}^+ - \bar{x}_i^+)^2 + \frac{1}{n^- - 1} \sum_{k=1}^{n^-} (x_{k,i}^- - \bar{x}_i^-)^2},$$

where \bar{x}_i is the mean value of characteristic i ; \bar{x}_i^+ and \bar{x}_i^- are the mean values of characteristic i among the positive and negative cases; and n^+ and n^- are the total numbers of positive and negative cases. We calculated the F-score for all the characteristics for the train dataset. The results are summarized in Tables 2 and 3 for the $\geq M1.0$ and $\geq X1.0$ class flares respectively. In Sec. 3 it was pointed out that the existence of threshold values is more prominent in the logarithmic scale for some characteristics. Therefore, we also calculated the F-scores of decimal logarithms of each parameter and used it if the score was higher than this for the normal-scaled characteristic (such cases are

Table 2. Importance of magnetic field characteristics for the forecast of \geq M1.0 class solar flares.

Characteristic	F-score	Fraction of negative cases below threshold, %	Total score	Decision
Area of PIL vicinity	1.71	0.64	1.00	Selected
PIL length	1.56	0.64	0.96	Selected
Total horizontal gradient at PIL vicinity (log)	1.51	0.64	0.94	Selected
Gradient-weighted PIL length (log)	1.50	0.64	0.94	Selected
Total flux at PIL vicinity (log)	1.47	0.63	0.92	Selected
R-mask (log)	1.41	0.62	0.90	Selected
Maximum gradient across PIL (log)	1.08	0.55	0.74	Discarded
Total AR flux	0.97	0.51	0.68	Discarded
Total AR area	0.84	0.44	0.59	Discarded
Total horizontal gradient in the AR	0.74	0.46	0.57	Discarded
Maximum field in the AR	0.30	0.27	0.30	Discarded

labeled by (log) in Tables 2 and 3). For these parameters, the logarithmic scale was also used for the SVM training.

Another method to judge the importance of a characteristic is to measure the fraction of negative samples that can be discarded based on some threshold value of the characteristic. In Sec. 3 we have already determined the thresholds above which 95% of flares occur. We apply the thresholds and summarize the fraction of negative cases below these thresholds in Tables 2 and 3. The results of both tests are normalized to the maximum score received for each test, summed up, and normalized once again. They are presented in the last columns of Tables 2 and 3. The first six characteristics in Tables 2 and 3, which have the highest scores, are included in the SVM training and testing procedures.

The existence of the thresholds allows us to classify large amounts of data before training the SVM: a case is automatically classified as negative if any of the six most discriminative characteristics is

Table 3. Importance of magnetic field characteristics for the forecast of $\geq X1.0$ class solar flares.

Characteristic	F-score	Fraction of negative cases below threshold, %	Total score	Decision
Total horizontal gradient at PIL vicinity	3.48	0.88	1.00	Selected
Total flux at PIL vicinity	3.12	0.86	0.94	Selected
PIL length	3.11	0.83	0.92	Selected
R-mask	2.69	0.88	0.89	Selected
Gradient-weighted PIL length	2.58	0.86	0.86	Selected
Total AR flux	2.37	0.88	0.84	Selected
Area of PIL vicinity	2.82	0.76	0.84	Discarded
Maximum gradient across PIL	2.46	0.76	0.78	Discarded
Total AR area	1.97	0.80	0.74	Discarded
Total horizontal gradient in the AR	1.64	0.74	0.65	Discarded
Maximum field in the AR (log)	0.83	0.49	0.41	Discarded

below the threshold. It was found that this procedure allows us to reduce the amount of data for the SVM classification by 72.0% (leaving less than 1/3 of the cases) for $\geq M1.0$ class flares and by 93.7% for $\geq X1.0$ class flares. Only 9% of positive cases for $\geq M1.0$ and 11.5% for $\geq X1.0$ class flare were left out.

4.3. Training of the SVM Classifier

Our approach is to utilize the Support Vector Machine (SVM, Cortes & Vapnik 1995) classifier for flare forecast using Python module “Scikit-Learn” (Pedregosa et al. 2011). The description of SVM can be found in Bobra & Couvidat (2015). The SVM finds a plane in the descriptor space, which optimally separates the positive and negative cases by solving the following functional minimization problem:

$$L = \frac{1}{2}||\omega||^2 + C \sum_{i=1}^m \epsilon_i \rightarrow \min,$$

$$y_i(\langle \omega, x_i \rangle + b) \geq 1 - \epsilon_i, \quad \epsilon_i \geq 0,$$

where ω is a vector normal to the separating plane; i is case number in the “train” dataset, varying from 0 to m ; C is a soft margin parameter; ϵ_i is a measure of misclassification of case i ; y_i is a constant equal to 1 for positive cases, and -1 for negative cases. After some transformations, this problem becomes a quadratic minimization problem: the functional depends only on scalar products of vectors of characteristics $\langle x_i, x_j \rangle$. To achieve better separation between the positive and negative cases, very often the so-called Kernel trick is used. The scalar product of characteristics in the functional is replaced by a function of the characteristics:

$$\langle x_i, x_j \rangle \rightarrow k(x_i, x_j).$$

In our prediction algorithm, we use the sigmoid SVM kernel which demonstrated the most promising results in the training phase:

$$k(x_i, x_j) = \tanh(\gamma \langle x_i, x_j \rangle + r),$$

where γ and r are tuning parameters. The other SVM parameters are the soft margin parameter and weights for both classes (multipliers of the soft-margin parameter). In our SVM tuning, we optimize all these parameters.

For the SVM training, we normalize the “train” dataset following [Nishizuka et al. \(2017\)](#): $Z = (X - \mu)/\sigma$, where X is a non-normalized data set, μ is the mean, and σ is the standard deviation. We use the same μ and σ parameters to normalize the “test” data set. To find the optimal SVM kernel and its parameters, we perform a cross-validation procedure on the “train” dataset: divide it into two subsets (one simulating the train data set, and one — the test data set) five times, and average the SVM results. As a measure of the SVM performance, we use the True Skill Statistics (TSS) metrics defined as:

$$TSS = \frac{TP}{TP + FN} - \frac{FP}{FP + TN},$$

where TP is the true positive prediction (number of positive cases predicted as positive), TN is the true negative prediction (number of negative cases predicted as negative), FP is the false positive prediction (number of negative cases predicted as positive), FN is the false negative prediction (number of positive cases predicted as negative). The TSS score is not sensitive to the class imbalance ratio (the relative number of positive and negative cases), and is zero for a pure negative prediction (when all cases are predicted as negative).

For the $\geq M1.0$ class solar flares, we found that the best score of $TSS = 0.70$ can be obtained using the “sigmoid” SVM kernel (described above) with parameters $C = 10000$, $\gamma = 0.001$ and $r = 0.1$, and negative/positive class weights of $1/20$. This score was derived from the following predictions: $TP = 1830$, $TN = 45788$, $FP = 7924$, $FN = 334$ (includes all the cases in the test dataset). The obtained TSS score is lower than one in the works of Bobra & Couvidat (2015, $TSS = 0.817$) and Nishizuka et al. (2017, $TSS = 0.88$ for SVM classifier). Nevertheless, it is higher than the known expert predictions mentioned by Nishizuka et al. (2017): $TSS = 0.50$ for the NICT Space Weather Forecasting Center and $TSS = 0.34$ for the Royal Observatory of Belgium (Devos et al. 2014).

For the $\geq X1.0$ class solar flares, we obtained $TSS = 0.64$ for the same “sigmoid” SVM kernel but with different parameters: $C = 1000$, $\gamma = 0.1$ and $r = 10.0$, and negative/positive classes weights of $1/50$. This TSS was derived from the following predictions: $TP = 198$, $TN = 51991$, $FP = 3603$, $FN = 84$. Nishizuka et al. (2017) received significantly higher TSS score for $\geq X1.0$ class flares ($TSS = 0.88$ for SVM classifier). Again, our results are higher than the expert prediction with $TSS = 0.21$ (the NICT Space Weather Forecasting Center, Nishizuka et al. 2017).

5. DISCUSSION AND CONCLUSION

In this paper, we have developed a machine-learning procedure solely based on the line-of-sight (LOS) magnetic field observations that are available in near-real time from space-based and ground-based observatories. The procedure is based on analysis of characteristics of the magnetic field Polarity Inversion Line (PIL) which is automatically identified by performing the magnetogram segmentation formulated as an optimization task. The PIL characteristics were derived from the SDO/HMI magnetograms for each AR with 1 h cadence. We estimated the importance of these char-

acteristics for forecasting $\geq M1.0$ and $\geq X1.0$ solar flares, and trained the Support Vector Machine (SVM) to maximize the True Skill Statistics (TSS) metrics. Finally, we can answer the two questions of this work.

1. *What characteristics of the LOS magnetic field are most important for the flare initiation and magnitude?* It was found that the PIL characteristics are more important for the forecasts rather than the global AR characteristics. The difference is especially evident for the $\geq M1.0$ class solar flares (see Table 2 for details), for which we found significant gap between the scores for the PIL characteristics (besides the Maximum Gradient across PIL) and the global characteristics. For the $\geq X1.0$ the PIL characteristics are still dominant, however, some global characteristics (especially the total AR unsigned magnetic flux) are comparably important. The local characteristics such as the Maximum Gradient across PIL and Maximum field magnitude receive significantly lower scores than the integrated characteristics. The scoring procedure was very intuitive: we determined the importance based on the fraction of non-flaring cases which we can cut off by applying a threshold (above which 95% of flares are expected), and on the distance between the positive and negative classes with respect to the standard deviations of these classes (Fisher ranking score).

2. *Is it possible to construct a reliable forecast of $\geq M1.0$ and $\geq X1.0$ class flares based only on the LOS magnetic field characteristics?* The answer is positive. We have received the $TSS = 0.70$ for prediction of $\geq M1.0$ class flares, and $TSS = 0.64$ for prediction of $\geq X1.0$ class flares which are higher than the mentioned expert-based predictions. However, the received scores are still lower than ones obtained by using characteristics of the vector magnetic field data ($TSS = 0.817$, Bobra & Couvidat 2015, $TSS = 0.88$ for SVM classifier, Nishizuka et al. 2017) and are accompanied by relatively high false positive predictions.

In our work, we have confirmed the particular importance of the Polarity Inversion Line regions in the flare development process. Despite the promising results, we should always keep in mind that the prediction is metrics-dependent. In this work, we maximize the True Skill Statistics in a single parameter setup, which resulted in high false positive prediction cases. Maximizing other metrics can result in other optimal SVM parameters and prediction scores (Bobra & Couvidat 2015).

Further work is needed to develop algorithms for quantitative prediction of the flare class and physical properties (eruptive or non-eruptive nature, geo-effectiveness etc).

Authors thank the GOES and SDO/HMI teams for the availability of high-quality scientific data. Authors also thank D. Laptev for valuable discussions of the magnetogram segmentation algorithm. The research was partially supported by the NASA Grants NNX14AB68G and NNX16AP05H.

REFERENCES

- Ahmed, O.W., Qahwaji, R., Colak, T. et al. 2013, SoPh, 283, 157
- Barnes, G., Leka, K.D., Schrijver, C.J. et al. 2016, ApJ, 829, 89
- Bishop, C. 2006, “Pattern Recognition and Machine Learning”, Springer, 55
- Bobra, M.G. and Couvidat, S. 2015, ApJ, 798, 135
- Chang, Yin-Wen, & Lin, Chih-Jen 2008, in JMLR: Workshop and Conf. Proc. 3, WCCI 2008 Workshop on Casualty (Brookline, MA: Microtone Publishing), 53
- Chernyshov, V., Laptev, D. and Vetrov, D. 2011, The 21st International Conference on Computer Graphics and Vision, Russia, Moscow, September 26-30
- Cortes, C., & Vapnik, V. 1995, Mach. Learn., 20, 273
- Devos, A., Verbeeck, C., & Robbrecht, E. 2014, JSWSC, 4, A29
- Emslie, A.G., Dennis, B.R., Shih, A.Y. et al. 2012, ApJ, 759, 71
- Falconer, D.A., Moore, R. L., Porter, J. G. et al. 1997, ApJ, 482, 519
- Falconer, D.A., Moore, R.L. and Gary, G.A. 2003, Journal of Geophysical Research (Space Physics), 108, 1380
- Falconer, D., Barghouty, A.F., Khazanov, I. and Moore, R. 2011, Space Weather, 9, S04003
- Falconer, D.A., Moore, R.L., Barghouty, A.F. and Khazanov, I. 2012, ApJ, 757, 32
- Falconer, D.A., Moore, R.L., Barghouty, A.F. and Khazanov, I. 2014, Space Weather, 12, 306
- Hagyard, M.J., Venkatakrishnan, P. and Smith, Jr., J.B. 1990, ApJS, 73, 159
- Jing, J., Song, H., Abramenko, V. et al. 2006, ApJ, 644, 1273
- Kosovichev, A.G. and Zharkova, V.V. 2001, ApJL, 550, L105
- Kumar, P., Yurchyshyn, V., Wang, H. and Cho, K.-S. 2015, ApJ, 809, 83
- Laptev, D. 2011, Specialist Dissertation “Search for Informative features on Solar Magnetograms”, Department of Computational Mathematics and Cybernetics, Moscow State University, Moscow, Russia
- Leka, K.D. and Barnes, G. 2003, ApJ, 595, 1277

- Leka, K.D. and Barnes, G. 2003, ApJ, 595, 1296
- Leka, K.D. and Barnes, G. 2003, ApJ, 656, 1173
- Mandage, R. S. and McAteer, R. T. J. 2016,
ArXiv e-prints, 1611.00830
- Mason, J.P. and Hoeksema, J.T. 2010, ApJ, 723,
634
- Nishizuka, N., Sugiura, K., Kubo, Y. 2017, ApJ,
835, 156
- Pedregosa, F., Varoquaux, G., Gramfort, A., et al.
2011, J. Mach. Learn. Res., 12, 2825
- Raboonik, A., Safari, H., Alipour, N. et al. 2016,
ArXiv e-prints, 1610.03222
- Scherrer, P.H., Schou, J. and Bush, R.I. 2012,
SoPh, 275, 207
- Schrijver, C.J. 2007, ApJL, 655, L117
- Severny, A.B. 1964, ARA&A, 2, 363
- Sharykin, I.N., Sadykov, V.M., Kosovichev, A.G.
et al. 2016, ArXiv e-prints, 1604.05380
- Stenflo, J. O. and Kosovichev, A. G. 2012, ApJ,
745, 129
- Sun, X., Hoeksema, J.T., Liu, Y., Kazachenko, M.
and Chen, R. 2017, ArXiv e-print 1702.07338
- Toriumi, S., Schrijver, C.J., Harra, L.K et al.
2016, ArXiv e-prints, 1611.05047
- Wang, H., Ewell, Jr., M.W., Zirin, H. and Ai, G.
1994, ApJ, 424, 436